Available online at www.sciencedirect.com

ScienceDirect

Acta Materialia 84 (2015) 506–514

Acta MATERIALIA

www.elsevier.com/locate/actamat

Effect of carbon on the coercivity and microstructure in fine-grained Nd–Fe–B sintered magnet

T.T. Sasaki,[a,*] T. Ohkubo,[a] Y. Une,[b] H. Kubo,[b] M. Sagawa[b] and K. Hono[a]

[a]*Elements Strategy Initiative Center for Magnetic Materials, National Institute for Materials Science, 1-2-1 Sengen, Tsukuba 305-0047, Japan*

[b]*Intermetallics Co., Ltd., Nagoya Creation Core 101&205, 2266-22 Anagahora, shimo-shidami, Moriyama-ku, Nagoya, Aichi 463-0003, Japan*

Received 4 August 2014; revised 17 October 2014; accepted 20 October 2014
Available online 5 December 2014

Abstract—We have investigated the effect of carbon on the coercivity and microstructure in fine-grained Nd–Fe–B sintered magnets fabricated by the pressless sintering method. The coercivity of the sample with the carbon content of 730 ppm (low-C) was 1.59 T while that of the sample with 1500 ppm (high-C) was 1.44 T in the as-sintered state. The low-C sample exhibited a larger coercivity increase by a post-sinter annealing, reaching the highest coercivity of 1.85 T, while the high-C sample reached a lower coercivity of 1.54 T. Detailed microstructure investigations using scanning electron microscopy, scanning transmission electron microscopy and atom probe tomography revealed that the high carbon content resulted in the formation of a Nd-carbide with a tetragonal structure and the reduction in the volume fraction of an α-Nd phase at triple junctions. This in turn decreased the Nd + Pr concentration in thin Nd-rich grain boundary phase, resulting in the lower coercivity.

Keywords: Nd–Fe–B; Sintered magnet; Coercivity; Microstructure

1. Introduction

(Nd, Dy)–Fe–B-based sintered magnets are currently used for traction motors and generators of (hybrid) electric vehicles because of their excellent combination of high maximum energy product, $(BH)_{max}$, and coercivity, $\mu_0 H_c$. However, there is a strong demand to achieve high coercivity without using Dy due to its scarcity and high cost. Grain size refinement is an effective way to increase the coercivity mainly because local stray fields can be reduced [1–10]. Apart from the grain size effect, impurities such as oxygen and carbon have been known to influence the coercivity [4,11]. The adverse effect of the impurities is more pronounced for grain sizes <3 μm, i.e. coercivity deviates from a logarithmic dependence on grain size for grain sizes <3 μm [11]. This is because the oxygen that is contaminated during jet-milling and subsequent powder metallurgy processing causes the oxidation of α-Nd phase, which hinders the formation of the continuous thin Nd-rich grain boundary phase [11]. By controlling the oxygen impurities using a pressless sintering (PLS) process, Une and Sagawa [12] reported that the logarithmic grain size dependence of sintered magnets can be extended to a grain size of 1 μm, in which they reported a coercivity of 2 T in Dy-free Nd–Fe–B sintered magnets.

Carbon is a contaminant from the organic lubricant, which is added for better alignment of the $Nd_2Fe_{14}B$ grains in the magnetic compaction, and the carbon impurity is known to be more sensitive to the coercivity compared to oxygen and nitrogen [13]; even the contamination of hundreds of ppm carbon causes a significant decrease in the coercivity. Although the distribution of carbon and its effect on the hard magnetic properties had been a subject of previous studies [13–15], it still remains unclear how the carbon impurity affects the microstructure and the coercivity of sintered magnets. In this work, we have revisited the effect of carbon on the microstructure and coercivity of fine-grained sintered magnets fabricated by the PLS process [12] using scanning electron microscopy (SEM), aberration-corrected high-angle annular dark-field scanning transmission electron microscopy (HAADF-STEM) and three-dimensional atom probe (3DAP).

2. Experimental procedure

Fine-grained sintered magnets with different carbon contents were prepared by the PLS process [12]. Helium jet-milling was used to crush the strip cast flakes with the chemical composition of $Fe_{bal.}Nd_{26.4}Pr_{4.1}B_{1.0}Cu_{0.1}Al_{0.28}Co_{0.9}$ into

* Corresponding author; e-mail: sasaki.taisuke@nims.go.jp

http://dx.doi.org/10.1016/j.actamat.2014.10.047
1359-6462/

powders with a mean diameter of 1.3 μm. The powders were consolidated at 920 °C for 2 h after a magnetic compaction. In order to reduce the carbon content, the green compact was heat treated at 400 °C in a hydrogen atmosphere to decompose and remove the organic lubricant from the sample prior to the sintering. Table 1 summarizes the chemical compositions and the density of the sintered samples. Hereafter, the samples containing 730 and 1500 ppm carbon are denoted as the low-C sample and the high-C sample, respectively. The as-sintered samples were then post-sinter annealed at 500 °C for 1 h. The magnetic properties of the samples were measured using a DC recording fluxmeter (Toei Industry Co., Ltd.).

SEM observation was performed using a Carl Zeiss Cross Beam 1540 EsB field emission microscope, equipped with an in-lens type detector and energy-dispersive spectroscopy (EDS) detector (Bruker XFlash 6 series). The SEM observation was performed for the surface milled by Ga-ion beam at an acceleration voltage of 2 kV. STEM observation was performed using a FEI Titan G^2 80–200 TEM with a probe aberration corrector. Thin foils for STEM observation were prepared by the lift-out technique using a focused ion beam/scanning electron (FIB/SEM) dual-beam microscope (FEI Helios Nanolab 650). 3DAP analyses were performed using a locally built laser-assisted wide-angle tomographic atom probe with an ultraviolet femtosecond laser of wavelength 343 nm. Needle-like specimen including the region of interest was lifted out using the FEI Helios Nanolab 650, and placed on a sharpened W wire, and fabricated into the needle shape using an annular Ga ion beam in the Carl Zeiss CrossBeam 1540 EsB.

3. Results

Fig. 1 shows the second quadrant of the magnetization curves of the low-C and high-C samples in as-sintered and post-sinter annealed conditions. Table 1 summarizes the magnetic properties of the samples. While all the samples show the same remanent magnetization ($\mu_0 M_r$) of 1.44 T, the coercivity of the as-sintered low-C sample (1.59 T) is higher than that of the as-sintered high-C sample (1.44 T). After the post-sinter annealing, the coercivity increased to 1.85 and 1.54 T for the low-C and high-C samples. The increase of the coercivity by the post-sinter annealing is larger in the low-C sample compared to the high-C sample, indicating that the carbon impurity substantially affects the coercivities in both as-sintered and optimally heat-treated samples.

Fig. 2 shows a backscattered electron (BSE) SEM image, in-lens secondary electron (IL-SE) SEM image, EDS elemental maps of Nd, Fe, and those for O and C obtained from an as-sintered high-C sample. Nd-rich phases are imaged with brighter contrast with respect to the $Nd_2Fe_{14}B$ matrix in both BSE (Fig. 2a) and IL-SE images (Fig. 2b). Among phase identification studies on the Nd-rich phase

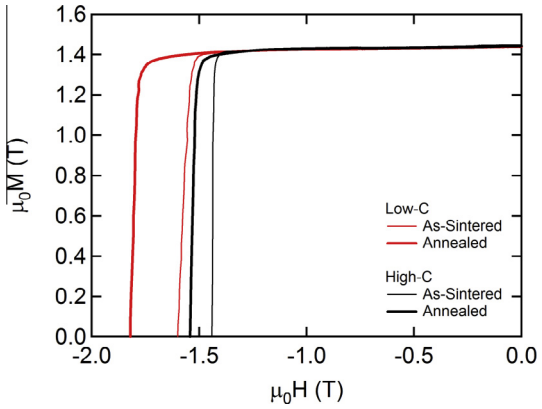

Fig. 1. Second quadrant of the magnetization curves for the samples.

located at the grain boundary triple junction [7,8,16–18], Sasaki et al. reported that the combination of the BSE and IL-SE images in SEM led to an unambiguous identification of the Nd-rich phase. Since the samples used in this work are fine-grained magnets with similar chemical composition fabricated by the PLS process as well as the one reported by Sasaki et al. [18], the phase constitution of the present samples should be same as the one reported previously [18]. Therefore, the Nd-rich phase can be identified based on the imaging contrast in the BSE and IL-SE SEM images and EDS elemental maps. The Nd-rich phase grains indicated by arrows 1 are identified as the α-Nd phase based on the EDS map. As we reported previously [18], the α-Nd phase exhibits the brightest contrast in the IL-SE image in which oxygen and carbon are not enriched, as shown in the EDS elemental map in Fig. 2e. The Nd-rich phase indicated by arrow 2 is the one with the $Ia\bar{3}$ structure, which is dimly imaged in the IL-SE SEM image, but has a brighter contrast compared to the α-Nd phase in the BSE SEM image. The Nd-rich phase indicated by arrow 3 is enriched in oxygen as shown in the oxygen elemental map in Fig. 2e and the EDS spectrum (Fig. 2f); hence, it is identified as face-centered cubic NdO_x [18]. From the imaging contrasts in the BSE and IL-SE images, the Nd-rich phase 4 was identified as the $NdFe_4B_4$ phase [18]. The Nd-rich phase indicated as 5 has an irregular shape compared to the other Nd-rich phases, which is darkly imaged compared to the NdO_x phase in the BSE image (Fig. 2a), while it shows a similar imaging contrast to the NdO_x phase in the IL-SE image (Fig. 2b). Note that carbon is enriched in this phase as shown in the EDS elemental map (Fig. 2e), and the EDS spectrum (Fig. 2f). Since Fig. 2e and f also show the presence of Fe in the carbon-enriched Nd-rich phase, we conclude that the carbon-enriched phase is a compound mainly consisting of Nd, Fe and C, probably a neodymium carbide (hereafter denoted as Nd-carbide).

Fig. 3 shows the bright-field TEM image and energy-filtered images for Nd, Fe and C of a post-sinter annealed

Table 1. Chemical composition of the samples.

	Chemical composition											Density
	wt.%								ppm			g/cm^3
	Nd	Pr	Dy	B	Cu	Al	Co	Fe	O	N	C	
Low-C	26.4	4.14	0.01	0.97	0.1	0.28	0.9	Bal.	1500	580	730	7.53
High-C									1600	580	1500	7.51